



**HAL**  
open science

# Pore-scale hydro-mechanical modeling of gas transport in coal matrix

Ahmad Mostafa, Luc Scholtes, Fabrice Golfier

► **To cite this version:**

Ahmad Mostafa, Luc Scholtes, Fabrice Golfier. Pore-scale hydro-mechanical modeling of gas transport in coal matrix. *Fuel*, 2023, 345, pp.128165. 10.1016/j.fuel.2023.128165 . hal-04213235

**HAL Id: hal-04213235**

**<https://uca.hal.science/hal-04213235v1>**

Submitted on 13 Nov 2023

**HAL** is a multi-disciplinary open access archive for the deposit and dissemination of scientific research documents, whether they are published or not. The documents may come from teaching and research institutions in France or abroad, or from public or private research centers.

L'archive ouverte pluridisciplinaire **HAL**, est destinée au dépôt et à la diffusion de documents scientifiques de niveau recherche, publiés ou non, émanant des établissements d'enseignement et de recherche français ou étrangers, des laboratoires publics ou privés.



Distributed under a Creative Commons Attribution - NonCommercial - NoDerivatives 4.0  
International License

# Pore-scale hydro-mechanical modeling of gas transport in coal matrix

Ahmad Mostafa<sup>1</sup>, Luc Scholtès<sup>2</sup>, Fabrice Golfier<sup>1</sup>

<sup>1</sup>Université de Lorraine, CNRS, Laboratoire GeoRessources, Nancy, France

<sup>2</sup>Université Clermont-Auvergne, CNRS, IRD, OPGC, Laboratoire Magmas et Volcans, Clermont-

Ferrand, France

Corresponding author email: [ahmad.mostafa@univ-lorraine.fr](mailto:ahmad.mostafa@univ-lorraine.fr)

## **ABSTRACT:**

We present a 3D model coupling a discrete element model and a pore network model specifically developed to describe the different diffusion mechanisms at stake in coal matrix as well as the associated adsorption induced deformations. The material is assumed to be saturated with gas and diffusion occurs through the combination of Knudsen diffusion within the pore space, surface diffusion at the solid surface, and adsorption-desorption at the pore-solid interface. The model is hydro-mechanically coupled in the sense that changes in pore pressure produce hydrostatic forces that deform the solid skeleton, while deformation of the pore space induces pore pressure changes that promote inter-pore flow. Sorption induced deformations are taken into account by considering an additional pressure term related to the concentration of gas within the medium (the so-called solvation pressure). The implemented transport models are verified against analytical solutions describing diffusion in porous media with and without sorption-desorption, and a comparison is made with a swelling experiment performed on a coal specimen to illustrate the relevance of the proposed approach for describing adsorption induced deformation. As a result, this new pore-scale model offers a precise way to assess coal matrix sorption induced deformation and contributes to the knowledge of CBM storage and transport processes.

Keywords: coal, gas transport, sorption, DEM, PNM, solvation pressure.

## 24 1 Introduction

25 Coalbed methane (CBM), also known as coal seam gas (CSG), has drawn much attention lately as an alternative  
26 energy resource. Production curves of CBM reservoirs are very different, however, from the ones of hydrocarbon  
27 conventional reservoirs (Liu et al., 2011). As emphasized by several studies (Li et al., 2017; Mostaghimi et al.,  
28 2017, 2016; Privalov et al., 2020; Wang et al., 2018), transport and poromechanical properties of coal are strongly  
29 driven by topological and morphological features of its pore space.

30 Coal is fractured by nature; it is a dual porosity/permeability system made up of a porous matrix surrounded by  
31 fractures known as cleats (Figure 1, scale II). The orientation of this quasi-orthogonal cleat network including  
32 tensile fractures or face cleats, and compressive and strike-slip fractures or butt cleats, depends on the principal  
33 stress' directions (Laubach et al., 1998) and provides preferential pathways for fluid flow with fracture apertures  
34 up to 100 microns. In contrast, methane gas is stored within the low porosity coal matrix with pore sizes generally  
35 varying from a few to several dozens of nanometers (Li et al., 2017; Wang et al., 2018).

36 The cleat-matrix system compartmentalizes the transport and mechanical properties of coal. Knudsen and surface  
37 diffusions prevail in the nanometer-sized pores of the matrix, while molecular diffusion and two-phase Darcy  
38 flow occur mainly within the cleat network. All these transport mechanisms induce mechanical couplings related  
39 to both (i) the pore pressure changes which may alter the effective stress and consequently impact the bulk volume  
40 of the coal and, (ii) the sorption processes which contribute to swell or shrink the coal matrix (Pini et al., 2009;  
41 Wang et al., 2011). Indeed, coal can sorb various gases including CO<sub>2</sub>, CH<sub>4</sub> and N<sub>2</sub>, and the adsorption of these  
42 gases induces swelling strains (Ceglarska-Stefańska and Czapliński, 1993; Ceglarska-Stefańska and Zarębska,  
43 2002; Pan and Connell, 2007). The magnitude of adsorption-induced deformation depends on the pores structure  
44 as well as on the nature of the gas adsorbed. It is well known for instance that the swelling is much higher with  
45 CO<sub>2</sub> than with CH<sub>4</sub> (Brochard et al., 2012), hence advocating the development of enhanced coal bed methane  
46 (ECBM) technology combining CBM recovery and CO<sub>2</sub> sequestration.

47 If many experimental studies have attempted to accurately determine this volumetric deformation rate (Majewska  
48 et al., 2010) and have given precious insights into the changes in pore size distribution during  
49 adsorption/desorption processes, they did not completely succeed to capture the dynamics of mass transfer within  
50 the cleat-matrix system since measurements are generally carried out at equilibrium (Wang et al., 2018). Also,

51 coal measurements are strongly affected by sample preparation, material composition, environment, and  
52 methodology (Mostaghimi et al., 2017).

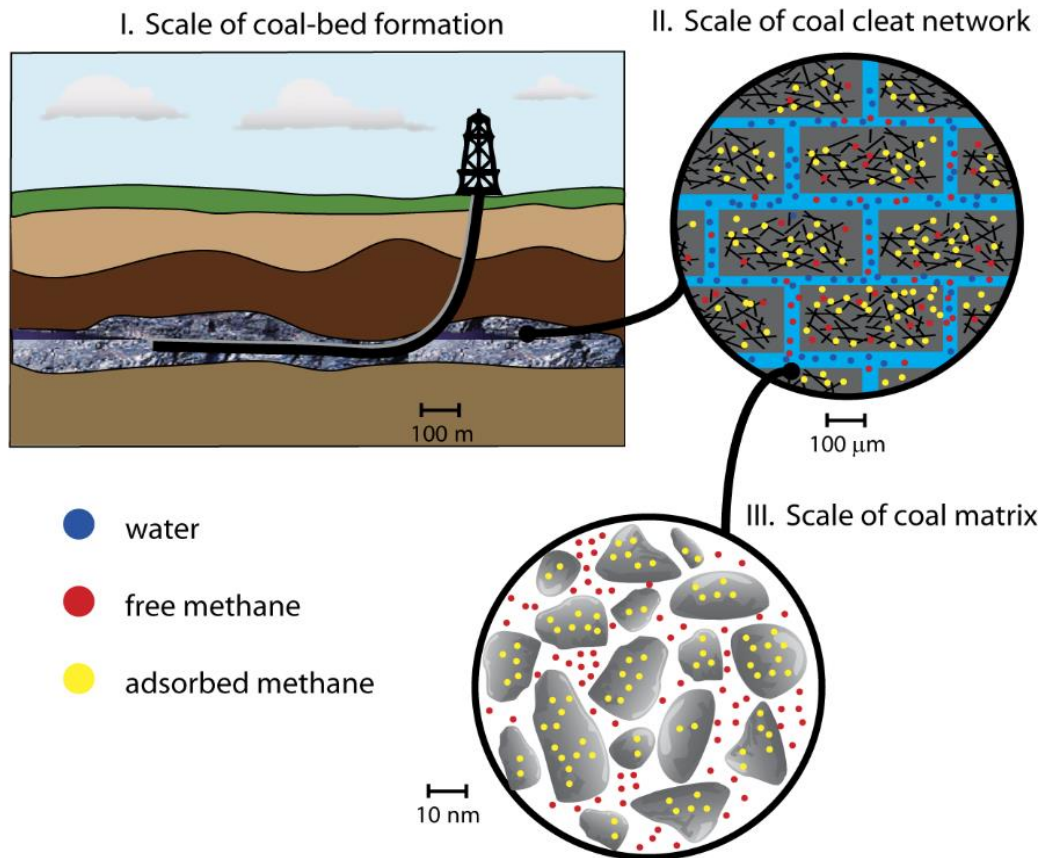
53

54 The inherent couplings between the physical processes at stake and the multiscale features of coal need to be  
55 explored further to better assess the macroscopic response of the coal matrix and the sorption induced volumetric  
56 deformation. If pioneering works (see for instance the review by (Liu et al., 2011)) have focused on permeability  
57 models using continuum (Connell, 2016; Guo et al., 2016) or dual-porosity approaches (Bertrand et al., 2017; Ma  
58 et al., 2017; Perrier et al., 2018; Wu et al., 2010), much attention has been paid in the last years to study the hydro-  
59 mechanical (HM) behavior of coal matrix at the pore-scale. For instance, Liu et al. (Liu and Mostaghimi, 2017)  
60 have derived a model based on the lattice Boltzmann method taking into account fluid-rock interactions with  
61 permeability and porosity variations to investigate the reactive transport of CO<sub>2</sub>-saturated brine in coal fractures.  
62 Youjun and Vafai, (Youjun and Vafai, 2017) have simulated fluid flow in pores using a digital SEM image of a  
63 coal rock sample. More recently, Sampath et al. (Sampath et al., 2020) have developed a HM model taking into  
64 account CO<sub>2</sub> diffusion and adsorption-induced mechanical deformation in coal matrix. To the best of our  
65 knowledge, however, a coupled HM model that incorporates the different transport mechanisms combining the  
66 diversity of nanoscale processes with the complexity of pore network topology has never been derived for coal  
67 matrix.

68 In this work, we propose a 3D pore-scale model for coal matrix based on a pore network model (PNM) describing  
69 gas transport coupled to a discrete element model (DEM) describing the mechanical behavior. The model is based  
70 on the framework of the pore scale finite volume (PFV) scheme implemented in the open-source platform YADE  
71 DEM (Šmilauer et al., 2015). The DEM-PFV coupled approach was initially designed for upscaling fluid flow in  
72 granular materials (Chareyre et al., 2012) and has been afterward used to describe hydro-mechanical processes in  
73 both soils (Catalano et al., 2014; Scholtès et al., 2015) and rocks (Papachristos et al., 2017). Lately, Caulk et al.  
74 (Caulk et al., 2020) extended its capability by incorporating heat transfer to the scheme and the associated  
75 possibility to describe thermo-hydro-mechanical processes. Here, we go further by introducing mass transport and  
76 sorption induced deformation processes to its formulation.

77 In summary, the equations governing the transport and HM schemes are first presented and derived accordingly  
78 to the geometric and numerical characteristics of the proposed model. Then, a validation exercise is provided

79 where each component of the transport model is challenged against analytical solutions of Fick's law considering  
 80 either pore-pore, pore-particle or particle-particle diffusion mechanisms. Finally, the coupled HM model is used  
 81 to simulate an experiment from the literature where a coal sample experience swelling due to gas adsorption.



82

83

Figure 1 Different scales of a coalbed reservoir.

## 84 2 Methodology

85 The porous coal matrix is modeled based on the assumption that the solid phase is made up of densely packed  
 86 spherical particles bonded one with another, and the pore space idealized as a network of interconnected pores.

87 The following sections detail the mechanical and transport models, the assumptions made and their respective  
 88 implementation in YADE DEM.

### 89 2.1 Mechanical scheme

90 The DEM is a numerical method that models geomaterials as assemblies of particles interacting one with another  
 91 according to predefined contact laws as initially proposed by Cundall and Strack (Cundall and Strack, 1979). Each  
 92 particle is defined through its own mass, size and position. The numerical scheme relies on an iterative temporal

93 integration of Newton's second law of motion to describe the movement of each particle depending on the forces  
 94 they are subjected to. To model coal, we use spherical particles and define elastic-brittle-force displacement laws  
 95 between the particles, as proposed in the bonded particle model (BPM) introduced by (Scholtès and Donzé, 2013)  
 96 to simulate rock like materials. The interaction force  $F$  between two particles  $a$  and  $b$  is decomposed into a normal  
 97 and a shear component.

98 The normal force is computed as:

$$99 \quad F_n = k_n \Delta D \quad (1)$$

100 where  $\Delta D$  is the relative displacement between  $a$  and  $b$ , and  $k_n$  is the normal stiffness defined by:

$$101 \quad k_n = E_{eq} \frac{R_a R_b}{R_a + R_b} \quad (2)$$

102 with  $E_{eq}$  an elastic modulus, and  $R_a$  and  $R_b$  the radii of  $a$  and  $b$  respectively. In compression,  $F_n$  can increase  
 103 indefinitely. In tension, a maximum acceptable force is defined as a function of the interparticle tensile strength  $t$   
 104 such as  $F_{n,max} = t A_{int}$ , with  $A_{int} = \pi[\min(R_a, R_b)]^2$ . If  $F_n \geq F_{n,max}$ , tensile rupture occurs.

105 The shear force is computed incrementally such as:

$$106 \quad F_s = \{F_s\}_{updated} + k_s \Delta u_s \quad (3)$$

107 with  $k_s$  the shear stiffness defined as  $k_s = P k_n$  with  $0 < P < 1$ , and  $\Delta u_s$  the relative incremental tangential  
 108 displacement.  $F_s$  can increase up to a threshold value defined by a Mohr-Coulomb type criterion such as  $F_{s,max} =$   
 109  $c + F_n \tan(\varphi)$ , with  $c$  the interparticle cohesion, and  $\varphi$  the interparticle friction angle. If  $F_s \geq F_{s,max}$ , shear rupture  
 110 occurs.

111 In addition, the integration of the equations of motion being done through an explicit finite difference scheme, a  
 112 local non viscous damping is used to dissipate kinetic energy and to ease the convergence of the simulated system  
 113 toward quasi-static equilibrium (see (Duriez et al., 2016) for details). Basically, the resultant force  $\vec{F} = \vec{F}_n +$   
 114  $\vec{F}_s$  considered in Newton's second law of motion is damped by a force  $\vec{F}^d$  defined as:

$$115 \quad \vec{F}^d = -\alpha \text{sign} \left( \sum \vec{F} \cdot \left( \vec{v} + \frac{\Delta t^m}{2} \vec{a} \right) \right) \sum \vec{F} \quad (4)$$

116 with  $\alpha$  a damping coefficient ( $0 < \alpha < 1$ ),  $\vec{v}$  and  $\vec{a}$  the velocity and acceleration of the particle respectively, and  
 117  $\Delta t^m$  the mechanical time step.

118 2.2 *Mass transport model*

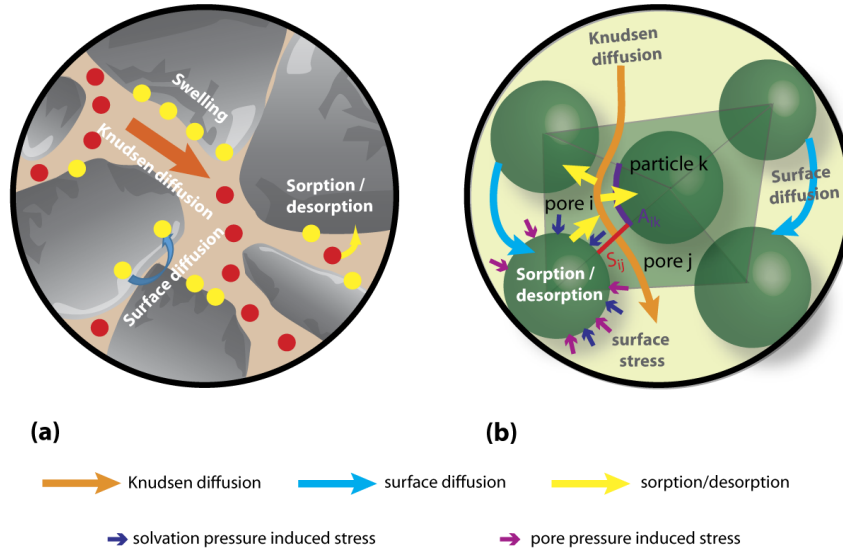
119 The diffusion of gas molecules within coal is rather complex due to the multi-scale architecture of the material,  
120 with pore sizes varying over several orders of magnitude (Jing et al., 2017). Theory of gas transport in porous  
121 media has a long history from the simple Fick's law for binary systems, to the Stefan-Maxwell equations for  
122 multicomponent mixtures and ultimately, the Dusty-Gas Model, based on the Chapman-Enskog kinetic theory  
123 and including the couplings between the various mechanisms (Reinecke and Sleep, 2002; Thorstenson and  
124 Pollock, 1989). Indeed, different transport modes manifest and drive gas migration in nanoporous media,  
125 depending on the pore size and on the flow regime (Do, 1998):

- 126 (i) Viscous flow in which displacement of molecules is induced by the mean velocity and governed by  
127 the total pressure gradient which acts as driving force.
- 128 (ii) Molecular or continuum diffusion where molecular-molecular collision prevails. In the gas mixture,  
129 each species moves relative to each other, and the driving force is the molar fraction gradient for an  
130 isothermal system.
- 131 (iii) Knudsen diffusion in which molecule-wall collisions dominate compared to collisions between  
132 molecules. Contrarily to molecular diffusion, each species moves independently from each other.  
133 The driving force here is the partial pressure gradient, which reduces to the total pressure gradient  
134 for a single species gas flow.
- 135 (iv) Surface diffusion in which adsorbed molecules moves along solid surface (pore walls) from one  
136 adsorption site to another (Choi et al., 2001).

137 These different transport mechanisms may compete and combine in a complex way. The relative magnitude of  
138 collisions between molecules relative to collisions between molecules and walls (molecular vs Knudsen diffusion)  
139 is classically expressed through the dimensionless Knudsen number  $K_n$ , defined as the ratio between the molecular  
140 mean free path length  $\lambda$  which is a function of pore pressure, and the mean pore diameter  $d$ . For nanoporous  
141 material such as coal, and at low pore pressures,  $K_n \gg 1$  typically, meaning that Knudsen diffusion generally  
142 prevails.

143 In the present study, we assume that water was previously expelled from coal matrix (residual water is expected  
144 to be trapped in the smallest pores that do not participate to flow) so that single-phase gas flow occurs within the  
145 pore network. The gaseous mixture is only composed of methane (an ideal gas assumption is employed) and a

146 part of gas is sorbed on the coal solid phase. Due to the very low permeability of the matrix and considering  
 147 single-species gas phase, only Knudsen and surface diffusions are thus considered (Figure 2a).



148

149

Figure 2 Mass transport and associated diffusion mechanisms in a) coal matrix, b) DEM-PFV model.

150 The DEM-PFV approach discretizes the pore space of the particle assembly into tetrahedra built from a weighted  
 151 Delaunay triangulation of the particles' centers (Figure 2b). Each tetrahedron contains both a solid fraction  
 152 resulting from the intersection between the tetrahedron and the associated vertex spheres, and a fluid fraction (the  
 153 pore) resulting from the remainder of the tetrahedron volume. Each pore is thus connected to 4 neighboring pores  
 154 and is in contact with 4 particles through surface areas where mass transport occurs by diffusion.

### 155 2.2.1 Mass balance equation for pores

156 Gas molecules are transported from one pore to another and are adsorbed/desorbed from and to the solid particles.  
 157 Let  $V_f$  be the volume of a pore  $i$  saturated with fluid (gas). Integrating the continuity equation in pore  $i$  gives:

$$158 \int_{V_f} \frac{\partial c_i}{\partial t} dV + \int_{V_f} \bar{\nabla} \cdot \bar{J}_{pore,i} dV = 0 \quad (5)$$

159 where  $c_i$  is the concentration of gas in pore  $i$ , and  $\bar{J}_{pore,i}$  represents the gas fluxes coming in and out of pore  $i$ .

160 Applying the divergence theorem to Equation (5) gives:

$$161 \int_{V_f} \frac{\partial c_i}{\partial t} \cdot dV + \int_{\partial V_f} \bar{J}_{pore,i} \cdot \bar{n} dS = 0 \quad (6)$$

162 Since each pore  $i$  is connected to 4 neighboring pores and in contact with 4 particles, the contour surface of each  
 163 pore can be calculated as:



164 
$$\partial V_f = \sum_{j=1}^4 \partial V_{pore,i-pore,j} + \sum_{k=1}^4 \partial V_{pore,i-particle,k} = \sum_{j=1}^4 S_{ij} + \sum_{k=1}^4 A_{ik} \quad (7)$$

165 with  $S_{ij}$  and  $A_{ik}$  the intersection surface areas between pore  $i$  and pore  $j$ , and between pore  $i$  and particle  $k$   
 166 respectively.

167 In our modeling approach, Knudsen diffusion describes the pore-pore diffusion fluxes and adsorption/desorption  
 168 describes the pore-particle diffusion fluxes (Figure 2). Equation (7) can then be written as follows:

169 
$$\int_{V_f} \frac{\partial c_i}{\partial t} dV = -\sum_{j=1}^4 \int_{S_{ij}} \bar{J}_{ij}^K \cdot \bar{n} dS - \sum_{k=1}^4 \int_{A_{ik}} \bar{J}_{ik}^{ad} \cdot \bar{n} dS \quad (8)$$

170 where  $\bar{J}_{ij}^K$  is the Knudsen diffusion flux between pore  $i$  and pore  $j$ , and  $\bar{J}_{ik}^{ad}$  is the adsorption/desorption flux  
 171 between pore  $i$  and particle  $k$ .

### 172 2.2.1.1 Knudsen diffusion

173 For a single-species phase flow along a straight circular capillary tube, the Knudsen diffusion flux can be defined  
 174 as (Do, 1998):

175 
$$\bar{J}^K = -D^K \bar{\nabla} c \quad (9)$$

176 
$$\bar{J}^K = -D^K \frac{1}{RT} \bar{\nabla} p$$

177 with  $p = cRT$  the gas pressure,  $R$  the gas constant (J/mol/K) and  $T$  the absolute temperature (K). The Knudsen  
 178 diffusion coefficient  $D^K$  (m<sup>2</sup>/s) is given by:

179 
$$D^K = \frac{2r}{3} \sqrt{\frac{8RT}{\pi M_g}} \quad (10)$$

180 with  $r$  the pore hydraulic radius, and  $M_g$  the molar mass (kg/m<sup>3</sup>).

181 The Knudsen flux may thus be written in terms of concentration between pore  $i$  and pore  $j$  such as:

182 
$$\bar{J}_{ij}^K = -\frac{2r}{3} \sqrt{\frac{8RT}{\pi M_g}} \bar{\nabla} c_{ij} \quad (11)$$

183 with  $r$  computed as proposed by (Chareyre et al., 2012) in the PFV scheme. Then the spatial integration of  
 184 Equation (11) between pores  $i$  and  $j$  gives:

185 
$$\int_{S_{ij}} \bar{J}_{ij}^K \cdot \bar{n} dS = - \frac{S_{ij}}{L_{ij}} \frac{2r}{3} \sqrt{\frac{8RT}{\pi M_g}} (c_j^t - c_i^t) \quad (12)$$

186 where  $L_{ij}$  is the distance between the centers of pore  $i$  and pore  $j$ .

187 2.2.1.2 Sorption

188 Sorption generally refers to the transport and attachment of a solute to the surface of a solid phase. Sorption  
 189 processes are usually investigated at equilibrium through isotherms that relate the amount of adsorbed solute to  
 190 the bulk concentration at constant temperature. In our modeling approach, we define kinetics formulations  
 191 balancing the relative rates of adsorption and desorption (Raouf et al., 2012).

192 ➤ **Linear first order sorption**

193 Linear sorption is characterized by an infinite number of sites on the particles' surfaces. As a result, solid particles  
 194 can adsorb an infinite number of gas molecules according to the following relation:

195 
$$\frac{\partial s}{\partial t} = (K_{att}c - K_{det}s) \quad (13)$$

196 where  $s$  (mol/m<sup>3</sup>) is the amount of solute adsorbed onto the solid phase surface,  $c$  (mol/m<sup>3</sup>) is the concentration  
 197 of solute in the mobile phase (gas),  $K_{att}$  and  $K_{det}$  are respectively the adsorption and desorption coefficients  
 198 defining the rate of adsorption/desorption, and  $t$  is the time (s). At equilibrium we recover the linear relationship:

199 
$$K_d = \frac{K_{att}}{K_{det}}$$

200 where  $\frac{\partial s}{\partial t} = 0$  then  $s = \frac{K_{att}}{K_{det}}c = K_d \cdot c \quad (14)$

201 ➤ **Langmuir sorption**

202 If adsorption is limited by the number of sites on the solid surface (Liu et al., 2019), the following nonlinear  
 203 relation can be used:

204 
$$\frac{\partial s}{\partial t} = \frac{s}{s_{max}} K_{det} - \left(1 - \frac{s}{s_{max}}\right) K_{att}c \quad (15)$$

205 where the sorption is proportional to the number of available sites  $\left(1 - \frac{s}{s_{max}}\right)$ ,  $s_{max}$  being the maximum amount  
 206 of sorbed concentration. At equilibrium, we recover:

207 
$$\frac{\partial s}{\partial t} = 0, \text{ then } \frac{s}{s_{max}} = \frac{K_d \cdot c}{1 + K_d c} \quad (16)$$

208 In our model, the diffusion fluxes between pores and particles can thus be described either by the linear relation  
 209 of Equation (13) or by the nonlinear relation (Langmuir isotherm) of Equation (15). For instance, the spatial  
 210 integration of the pore-particle diffusion flux between pore  $i$  and particle  $k$  in the case where it is governed by the  
 211 Langmuir isotherm is defined as:

212 
$$\int_{A_{ik}} \bar{J}_{ik}^{ad} \cdot \bar{n} dS = \frac{A_{ik}}{A_k} \left[ K_{det} \frac{s_k^t}{s_{k,max}} - \left( 1 - \frac{s_k^t}{s_{k,max}} \right) K_{att} c_i \right] \times V_p \quad (17)$$

213 where  $s_k$  (mol/m<sup>3</sup>) is the solute concentration adsorbed on the surface of particle  $k$ ,  $A_k$  is the overall surface of  
 214 particle  $k$ , and  $V_p$  is the volume of particle  $k$ .

215 Finally, considering both sorption Equation (17) and Knudsen diffusion Equation (12), the evolution of each pore  
 216 concentration is obtained by an explicit integration over time such as:

217 
$$c_i^{t+\Delta t} = \sum_{i=1}^4 \frac{V_p A_{ik}}{V_f A_k} \left[ \left( 1 - \frac{s_k^t}{s_{k,max}} \right) K_{att} c_i^t - K_{det} \frac{s_k^t}{s_{k,max}} \right] \Delta t^{\frac{ad}{des}} + \sum_{i=1}^4 \frac{S_{ij}}{V_f L_{ij}} \frac{2r}{3} \sqrt{\frac{8RT}{\pi M_g}} (c_j^t - c_i^t) \Delta t^K + c_i^t \quad (18)$$

218 with  $\Delta t^{\frac{ad}{des}}$  and  $\Delta t^K$  the associated time steps.

### 219 2.2.2 Mass balance equation for particles

220 The amount of gas molecules adsorbed on the solid particles results from the transport of gas molecules both from  
 221 neighboring solid particles and from pores (Figure 2b). Particle-particle flux occurs by surface diffusion, while  
 222 pore-particle flux results from adsorption/desorption process. Let  $V_p$  be the volume of a particle  $k$ . Integrating the  
 223 mass balance equation on particle  $k$  gives:

224 
$$\int_{V_p} \frac{\partial s_k}{\partial t} dV + \int_{V_p} \bar{\nabla} \cdot \bar{J}_{particle,k} dV = 0 \quad (19)$$

225 where  $s_k$  is the adsorbed concentration on particle  $k$ , and  $\bar{J}_{particle,k}$  represents the gas fluxes coming in and out of  
 226 particle  $k$ .

227 Applying the divergence theorem to Equation (19) gives:

228 
$$\int_{V_p} \frac{\partial s_k}{\partial t} dV + \int_{\partial V_p} \bar{J}_{particle,k} \cdot \bar{n} dS = 0 \quad (20)$$

229 Since each particle is connected to  $N$  particles ( $N$  depends on the spatial arrangement of the particles within the  
230 medium), and to 4 pores, the contour surface of each particle can be calculated as:

231 
$$\partial V_p = \sum_{l=1}^N \partial V_{particle,k-particle,l} + \sum_{i=1}^4 \partial V_{particle,k-pore,i} = \sum_{l=1}^N S_{kl} + \sum_{i=1}^4 A_{ik} \quad (21)$$

232 where  $S_{kl}$  is the intersection surface area between particle  $k$  and particle  $l$ , and  $A_{ki}$  is the intersection surface area  
233 between particle  $k$  and pore  $i$  (Figure 2b).

234 Equation (21) can then be written as follows:

235 
$$\int_{V_p} \frac{\partial s_k}{\partial t} dV = - \sum_{l=1}^N \int_{S_{kl}} \bar{J}_{kl}^S \cdot \bar{n} dS - \sum_{i=1}^4 \int_{A_{ki}} \bar{J}_{ki}^{ad} \cdot \bar{n} \cdot dS \quad (22)$$

236 where  $\bar{J}_{kl}^S$  is the surface diffusion flux between particle  $k$  and particle  $l$ , and  $\bar{J}_{ki}^{ad}$  is the adsorption/desorption flux  
237 between particle  $k$  and pore  $i$ .

#### 238 2.2.2.1 Surface diffusion

239 Particle-particle flux is governed by surface diffusion in which gas molecules are transported from the surface of  
240 a grain to the surface of a neighboring grain. In essence, molecules jump from an adsorption site to another  
241 adsorption site. The diffusive flux is thus driven by the gradient of sorbed concentration between and within  
242 particles and the surface diffusion flux can be expressed as:

243 
$$\bar{J}^S = -D^S \bar{\nabla} s \quad (23)$$

244 The surface diffusion coefficient  $D^S$  is known to be a function of temperature following the Arrhenius equation  
245 and strongly depends on the surface loading (Do, 1998). For sake of simplicity, however, it will be kept constant  
246 hereafter.

247 The spatial integration of the diffusive flux between particles  $k$  and  $l$  is defined as:

248 
$$\int_{S_{kl}} \bar{J}_{kl}^S \cdot \bar{n} dS = - \theta \frac{D^S S_{kl}}{L_{kl}} (s_k^t - s_l^t) \quad (24)$$

249 where  $S_{kl}$  is the intersection surface area between particle  $k$  and particle  $l$  computed here as  $S_{kl} = 4r_l r_k$ ,  $L_{kl}$  is the  
250 distance between the centers of particle  $k$  and particle  $l$ ,  $r_l$  and  $r_k$  are the radiuses of particle  $k$  and particle  $l$ ,

251 and  $\theta$  is a scaling parameter enabling to constrain the transport properties of the simulated medium depending on  
 252 the structural characteristics of the particle assembly ( $\theta$  is related to the particle connectivity which is a function  
 253 of the particle size distribution of the packing as well of its porosity).

#### 254 2.2.2.2 Sorption

255 Particle-pore diffusion processes are governed by the same mechanisms than pore-particle diffusion processes  
 256 (see Equation (17)).

257 Finally, combining both sorption Equation (17) and surface diffusion Equation (24), the evolution of each particle  
 258 concentration is obtained by an explicit integration over time such as:

$$259 \quad s_k^{t+\Delta t} = \sum_{i=1}^4 \frac{A_{ik}}{A_k} \left[ \left( 1 - \frac{s_k^t}{s_{k,max}} \right) K_{att} c_i^t - K_{det} \frac{s_k^t}{s_{k,max}} \right] \Delta t^{\frac{ad}{des}} + \sum_{l=1}^m \theta \frac{D^S S_{kl}}{V_p L_{kl}} (s_k^t - s_l^t) \Delta t^{sd} + s_k^t \quad (25)$$

260 with  $\Delta t^{\frac{ad}{des}}$  and  $\Delta t^{sd}$  the associated time steps.

### 261 2.3 Hydro-mechanical coupling

262 The hydraulic forces acting on a solid particle immersed in a fluid result from both the pressure and viscous stress  
 263 acting on its surface (Chareyre et al., 2012). In coal matrix with nanometer pores, pore velocities are very low  
 264 (they are actually neglected in the mass transport model) and hence are the viscous stress forces. We thus only  
 265 consider the contribution of the normal pressure forces which result from pressure losses within the pore space as  
 266 follows:

$$267 \quad \vec{F}_{ij}^k = A_{ij}^k (p_i - p_j) \vec{n}_{ij} \quad (26)$$

268 where  $p_i - p_j$  represents the pressure difference between pore  $i$  and pore  $j$ ,  $A_{ij}^k$  is the intersection surface area  
 269 between particle  $k$  and the pore throat between pore  $i$  and pore  $j$ ,  $\vec{n}_{ij}$  is the unit vector pointing from pore  $i$  to pore  
 270  $j$ . As shown in (Catalano et al., 2014) and in (Scholtès et al., 2015), the HM coupling resulting from Equation (26)  
 271 enables the DEM-PFV model to simulate conventional poromechanical behaviors as described by Biot's theory  
 272 (Biot, 1941).

273 The classical Biot's theory states that the mechanical behavior of a porous medium depends on the bulk fluid  
 274 pressure only ( $p_f$ ) without considering its detailed composition. This means that two pore fluids with different  
 275 compositions having the same bulk pressure should produce the same volumetric deformation. This is not verified

276 for swelling materials like coal which shows different deformation amplitudes depending on the nature of the pore  
 277 fluid (Ottiger et al., 2008). It is now well known that the deformation of coal is not solely governed by the pore  
 278 bulk pressure: as for all swelling materials, sorption processes induce additional deformation related to the nature  
 279 of the sorbed molecules (Brochard et al., 2012). Gas molecules get adsorbed at the surface of the pores and induces  
 280 a surface excess free energy. An additional interfacial force is thus exerted and resulting stress develops within  
 281 the porous medium. Different approaches were proposed to introduce these nanoscale features into an extended  
 282 poromechanical equation to explain the sorption-induced deformations from a continuum description. First works  
 283 have introduced the so-called solvation pressure to describe swelling since in confined pores, pressure is not  
 284 anymore a scalar (Gor and Neimark, 2010; Kowalczyk et al., 2008; Ustinov and Do, 2006; Yang et al., 2010). A  
 285 second class of models, based on an energy balance approach, relates the changes in surface potential energy  
 286 due to gas adsorption to the elastic energy (“Dilatation of Porous Glass - SCHERER - 1986 - Journal of the  
 287 American Ceramic Society - Wiley Online Library,” n.d.; Dolino et al., 1996; Grosman and Ortega, 2008; Pan  
 288 and Connell, 2007). Other researchers also have reformulated the poroelastic constitutive equations by introducing  
 289 an apparent porosity and an interaction free energy that are both related to the Gibbs adsorption isotherm (Mushrif  
 290 and Rey, 2009; Perrier et al., 2018; Pijaudier-Cabot et al., 2011; Sampath et al., 2020; Vermorel and Pijaudier-  
 291 Cabot, 2014). In contrast, Vandamme and co-workers (Brochard et al., 2012; Espinoza et al., 2014, 2013;  
 292 Nikoosokhan et al., 2014) have made use of the bulk pressure and of the swelling strain to express the sorbed  
 293 amount or the adsorption-induced pressure.

294 In the present work, the sorption-induced deformations are interpreted in terms of the solvation pressure or  
 295 adsorption pressure  $p_s$ , that is related to the amount of gas molecules attached to the solid skeleton. Specifically,  
 296 the total pore pressure in each pore  $i$  is equal to the sum of the bulk fluid pressure  $p_f$  and of the solvation pressure  
 297  $p_s$  such as:

$$298 \quad p_i = p_{i,f} + p_{i,s} \quad (27)$$

299 with  $p_{i,f}$  and  $p_{i,s}$  defined as follows:

300 
$$p_{i,s} = \sum_{k=1}^4 \frac{A_{i,k} \times p_s^k}{A_{i,k}} \quad (28)$$

301 
$$p_{i,f} = c_i RT \quad (29)$$

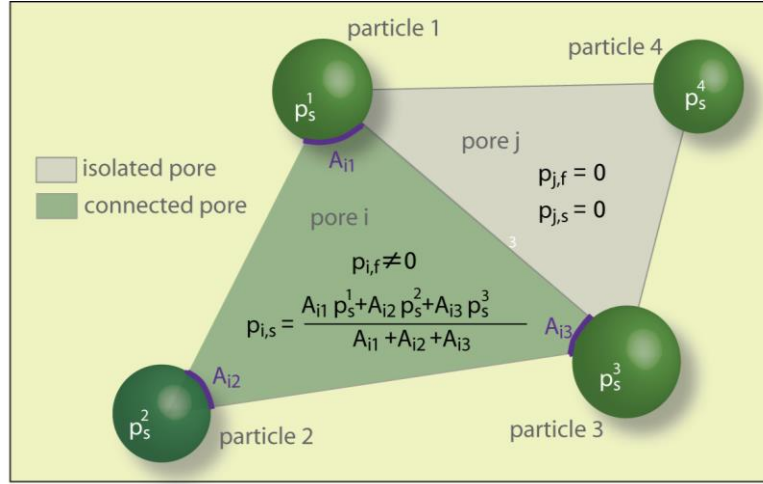
302 where the solvation pressure related to the amount of gas molecules attached to the particle  $k$  is denoted  $p_s^k$  and  
 303 computed as

304 
$$p_s^k = \alpha s_k RT \quad (30)$$

305  $A_{ik}$  is the intersection surface area between particle  $k$  and pore  $i$ , and  $\alpha$  is a coupling coefficient. Hereafter,  $\alpha$  is  
 306 fixed constant but it is not necessarily the case (Brochard et al., 2012).

307 Although the solvation pressure is dependent of the adsorbed amount on a grain and hence should be specific to  
 308 a given particle, it is also a pressure which is summed up with the bulk pressure specific to a pore. To further  
 309 explain how this additional pressure term is calculated within the pore space, we illustrate in Figure 3 the different  
 310 situations that can be encountered:

- 311 • Case 1: for connected pores (belonging to the connected porosity which will be further discussed in  
 312 Section 3), we compute a contact surface weighted average solvation pressure for each particle in contact  
 313 with pore  $i$ , and the fluid pressure value depends on the gas pressure gradient within the percolating pore  
 314 space.
- 315 • Case 2: for isolated pores (belonging to the unconnected porosity), the fluid pressure and the solvation  
 316 pressure are fixed to zero resulting in a zero-total pore pressure. These pores also have no contribution  
 317 on the fluxes related to the surrounding pores and particles.



318

319

Figure 3 2D representation of pore pressure distribution within the pores of the DEM-PFV

320

model: distinction between connected pores and unconnected pores

### 321 3 Model implementation

#### 322 3.1 Scaling strategy

323 If the interparticle properties presented in Section 2.1 can be calibrated so that the emergent mechanical properties  
 324 of the DEM model match those of the material to model (see (Scholtès and Donzé, 2013) for details of the  
 325 procedure), the diffusion mechanisms at stake require some adjustments of the transport model. For instance, coal  
 326 matrix has a porosity that is significantly smaller than the porosity of an assembly of spherical particles. Basically,  
 327 the pore space of the model is scaled so that the effective volume of fluid is  $V_{f,eff}$  equal to:

$$328 \quad V_{f,eff} = V_f \frac{n_m}{n_a} \quad (31)$$

329 with  $n_a$  the porosity of the spherical particle assembly, and  $n_m$  the porosity of the actual material.

330 Scaling the diffusive fluxes is actually sufficient to match the required porosity without changing the volume of  
 331 both the pore space and the solid phase in the discretized equations, resulting in a total mass balance that accurately  
 332 represents the material to model as follows:



333 For particles: 
$$\bar{J}_{eff} = \bar{J} \frac{1-n_a}{1-n_m} \quad (32)$$

334 For cells: 
$$\bar{J}_{eff} = \bar{J} \frac{n_a}{n_m} \quad (33)$$

335 with  $\bar{J}$  the non-scaled flux calculated according to the previous sections and  $\bar{J}_{eff}$  the effective (“scaled”) diffusive  
336 flux.

337 In addition, we also introduced a procedure to adjust the poromechanical response of our DEM-PFV model since  
338 the Biot coefficient of a DEM assembly is intrinsically equal to 1 given the rigid particle assumption of the DEM  
339 formulation. As a matter of fact, according to the poroelasticity theory (Detournay and Cheng, 1993), the  
340 contribution of the pore pressure  $p$  to the overall deformation of porous media is defined through the effective  
341 stress such as

342 
$$\sigma' = \sigma - bp \quad (34)$$

343 where  $\sigma'$  is the effective stress,  $\sigma$  is the total stress, and  $b$  is the Biot coefficient equal to  $1 - \frac{K}{K_s}$  with  $K$  the bulk  
344 modulus of the medium, and  $K_s$  the bulk modulus of the solid phase. This effective stress produces volumetric  
345 strain  $\varepsilon_v$  which, for a swelling material, presents an additional term of adsorption induced strain  $\varepsilon_s$  as follows:

346 
$$\varepsilon_v = -\frac{1}{K}(\sigma - bp_f) + \varepsilon_s \quad (35)$$

347 where  $\sigma = \frac{\sigma_{kk}}{3}$  is the mean stress and  $\varepsilon_s$  is defined such as:

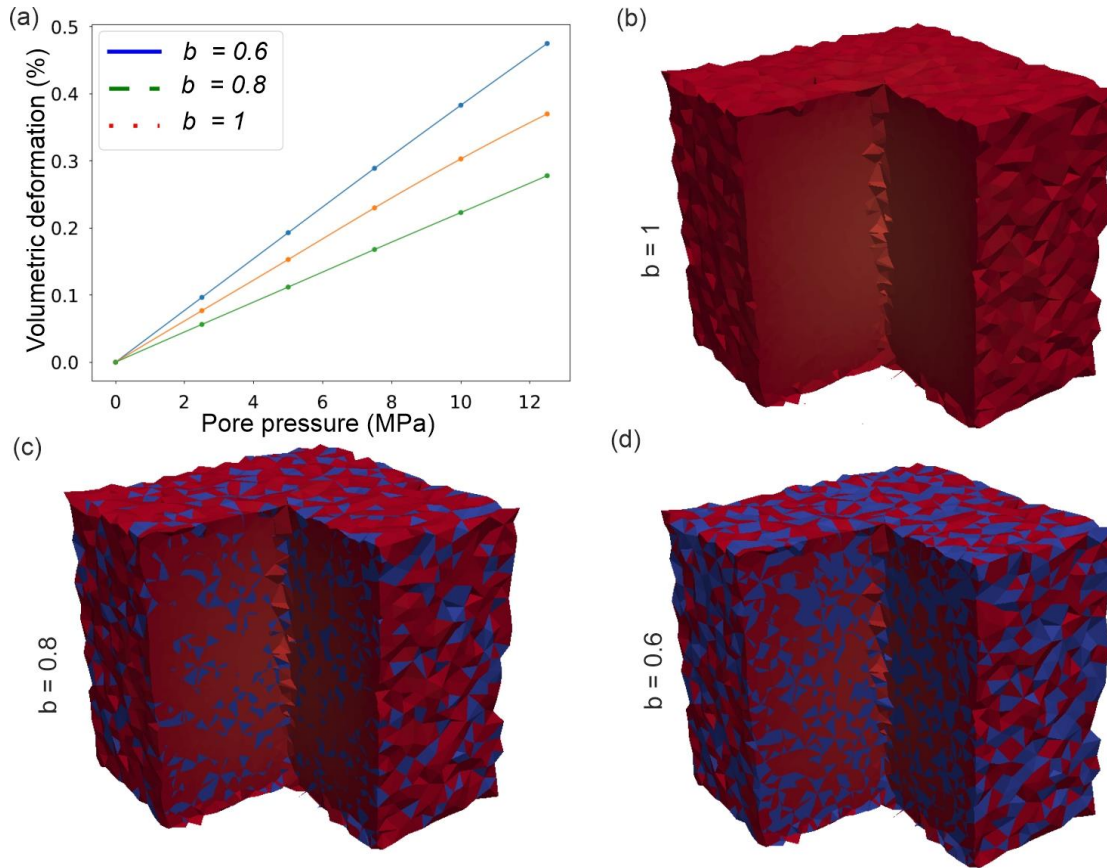
348 
$$\varepsilon_s = b \frac{ps}{K} \quad (36)$$

349 Instead of applying a global scaling factor to Equation (27), we introduced the possibility to neutralize a certain  
350 amount of pores within the pore network so that the connected porosity of the particle assembly  $n_{a,c}$  is equal to:

351 
$$n_{a,c} = bn_a \quad (37)$$

352 with  $b$  directly equal to the Biot coefficient of the material. The neutralized pores (unconnected porosity)  
353 correspond to tetrahedra randomly chosen within the triangulated mesh where gas transport calculations are  
354 simply not performed. These isolated pores thus participate to the overall deformability of the particle assembly

355 due to their compliance without contributing to its poromechanical response as illustrated in Figure 4.



356

357 Figure 4 Illustration of the connected porosity  $n_{ac}$  and of its effect on the Biot coefficient, Equation (37): a) Volumetric deformation  
 358 as a function of pore pressure increase and b,c,d) pressure distribution at equilibrium ( $p_{c\infty}=12.5$  MPa) in numerical samples with  
 359 different pre-defined Biot coefficients (the connected pores are in red and the isolated pores in blue).

360 **3.2 Numerical stability**

361 Numerical stability needs to be considered in every explicit numerical scheme as any effect can only move by a  
 362 maximum of one spatial grid block in one time step. For instance, in the general case of a 2D diffusion problem,  
 363 the explicit discretization reads:

364 
$$\frac{u_i^{t+\Delta t} - u_i^t}{\Delta t} = D \frac{u_{i+1}^t - 2u_i^t + u_{i-1}^t}{\Delta x^2} \quad (38)$$

365 where  $D$  is the diffusion coefficient. Solving Equation (38) for  $u_i^{t+\Delta t}$  leads to:

366 
$$u_i^{t+\Delta t} = ru_{i+1}^t + (1 - 2r)u_i^t + ru_{i-1}^t \quad (39)$$

367 with  $r = D \frac{\Delta t}{\Delta x^2}$  the Fourier Number. Applying the Von Neumann stability analysis, the FTCS (Forward Time  
368 Centered Space) method is satisfied only if the following condition is fulfilled:

369 
$$r \leq \frac{1}{2} \text{ then } \Delta t \leq \frac{\Delta x^2}{2D} \quad (40)$$

370 In our model, in addition to the mechanical time step that governs the solid particles motion, three-time steps exist  
371 due to the three different types of transport mechanisms occurring respectively between pore-pore, pore-particle  
372 and particle-particle. To ensure the stability of the numerical scheme, the simulation time step  $\Delta t$  is set up equal  
373 to a fraction of the minimum time step  $\Delta t_{min} = \min\left(\Delta t^m, \Delta t^K, \Delta t^{des}, \Delta t^{sd}\right)$  required to ensure the stability of the  
374 numerical scheme (in all our simulations, the time step was defined equal to  $0.8 \Delta t_{min}$ ).

#### 375 **4 Verification of the transport models**

376 To verify the correct implementation of the transport equations in our DEM-PFV model, we compared its  
377 predictions to analytical solutions of Fick's law considering different 1D problems. For that purpose, we built up  
378 a pseudo 1D numerical assembly with dimensions equal to  $L_0 \times 0.2L_0 \times 0.2L_0$  m, made up of 1,000 particles with  
379 radii varying between 7.1 and 13 mm, and 5,500 cells. In all the verification examples presented below, HM  
380 couplings were not considered, and the simulated medium was non deformable (the mechanical scheme was  
381 turned off and the particles fixed in space and time). In the present section and for the sake of comparison, all  
382 results and variables will be presented dimensionless. The  $x$ -coordinate, the Knudsen diffusion coefficient  $D^K$  and  
383 the concentration  $c$  are normalized respectively by the sample length  $L_0$ , the gas diffusion coefficient  $D_0$  and the  
384 inlet concentration  $c_0$ . The dimensionless time is defined as  $t = Dt_0 / L^2$  where  $t_0$  is the physical time. Similar  
385 normalization holds for the sorbed concentration  $s$  and the surface diffusion coefficient  $D^s$ . The different test cases  
386 with the corresponding parameter values used in the simulations and analytical solutions are gathered in Table 1.

387

388

389 Table 1.

390 Numerical parameters of the different verification test cases.

Parameter	Test case 1	Test case 2	Test case 3
$n$	0.45	0.47	0.45
Dimensionless time step $\Delta t$	9e-7	9e-6	9e-7
$D^K/D_0$	1	-	1
$D^S/D_0$	-	1	-
$\theta$	-	1.12	-
$K_d = k_{att}/k_{det}$	-	-	2
$k_{att}$	-	-	0.116
$k_{det}$	-	-	0.058

391 4.1 Test case 1: Knudsen diffusion

392 First, we consider diffusion of non-sorbing species within a nanoporous material. As a consequence, only Knudsen  
393 diffusion occurs, and both sorption and surface diffusion may be neglected. The boundary value problem is thus  
394 defined by the following initial and boundary conditions:

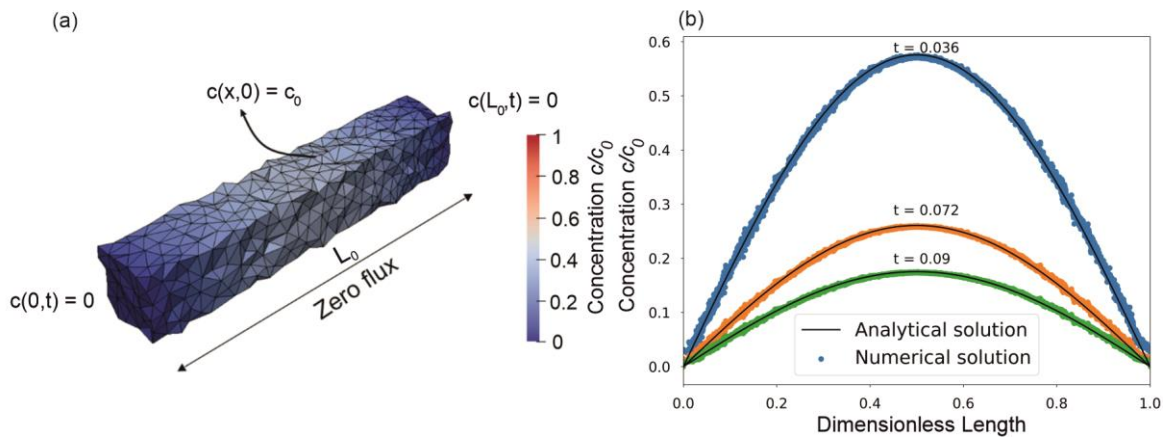
$$395 \quad \frac{\partial c}{\partial t} = D^K \frac{\delta^2 c}{\delta x^2}, \quad \forall x \in [0, L_0] \quad (41)$$

$$396 \quad \begin{aligned} c(x, 0) &= c_0, \quad \forall x \in [0, L_0] \\ c(0, t) &= c(L_0, t) = 0 \end{aligned}$$

397 Using Fourier series, the unsteady solution of this 1D diffusion problem can be written as follows:

$$398 \quad c(x, t) = \sum_{m=1}^{\infty} \frac{2}{\pi} \left( \frac{1 - \cos(m\pi)}{m} \right) \sin \left( m\pi \frac{x}{L_0} \right) e^{-\frac{D^K}{n_a L_0^2} (m\pi)^2 t_0} \quad (42)$$

399 The numerical assembly, illustrated in Figure 5a, was subjected to the initial and boundary conditions defined in  
400 Equation (41) and the simulation was run with the parameters presented in Table 1.



401  
402 Figure 5 a) Concentration distribution in pores at  $t=0.04$ . b) Numerical and analytical concentration profiles in pores at different times.

403 As shown in Figure 5b, the concentration distribution in the numerical model matches perfectly the analytical  
 404 solution in space and time, confirming the accuracy of the numerical scheme for simulating Knudsen diffusion.

#### 405 4.2 Test case 2: surface diffusion

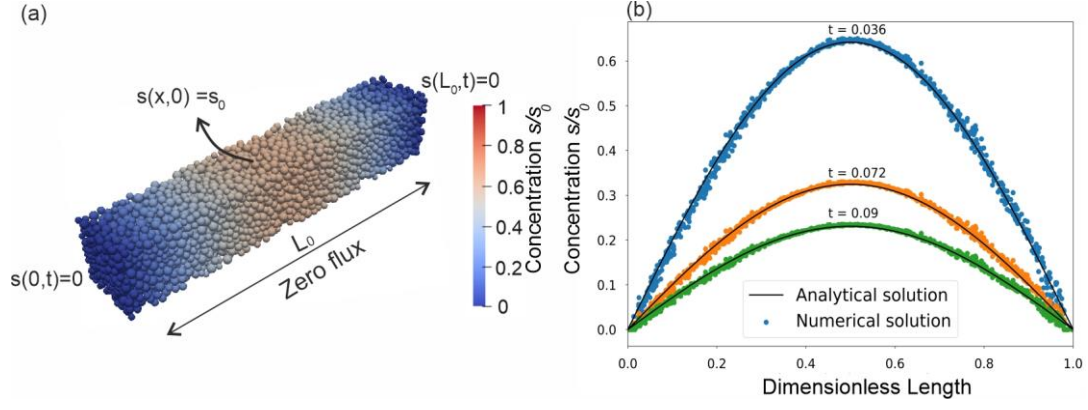
406 The second test case assumes that the gaseous species is now irreversibly adsorbed and may only diffuse through  
 407 the solid grains. Surface diffusion is thus considered as the only effective transport mechanism and the problem  
 408 is defined by the following initial and boundary conditions:

$$\begin{aligned}
 409 \quad \frac{\partial s}{\partial t} &= D^s \frac{\delta^2 s}{\delta x^2}, \quad \forall x \in [0, L_0] \\
 410 \quad s(x, 0) &= s_0, \quad \forall x \in [0, L_0] \\
 411 \quad s(0, t) &= s(L_0, t) = 0
 \end{aligned} \tag{43}$$

412 This 1D diffusion problem is very similar to the first one and the analytical solution in terms of Fourier series can  
 413 be written as follows:

$$414 \quad s(x, t) = \sum_{m=1}^{\infty} \frac{2}{\pi} \left( \frac{1 - \cos(m\pi)}{m} \right) \sin \left( m\pi \frac{x}{L_0} \right) e^{-\left( \frac{D^s}{(1-n_a)L_0^2} \right) (m\pi)^2 t_0} \tag{44}$$

415 The numerical values used in the simulation are presented in Table 1. The parameter  $\theta$  was initially calibrated  
 416 since the number of contacts between particles depends on the packing characteristics (samples are generated  
 417 using a random packing procedure, considering a pre-defined size distribution). Figure 6a displays an example of  
 418 the concentration field in the solid grains at a given time of the simulation, while a comparison of the numerical  
 419 solutions with averaged concentration profiles at different times is provided in Figure 6b. As for test case 1, the  
 420 concentration distribution in the numerical model matches perfectly the analytical solution in space and time,  
 421 showing the correctness and reliability of our surface diffusion model and of its implementation.



422

423 Figure 6 Concentration distribution in particles at  $t = 0.04$ . b) Comparison of numerical and analytical concentration profiles in particles at  
424 different times.

### 425 4.3 Test case 3: Knudsen diffusion with adsorption/desorption

426 For this test case, we consider diffusion of a sorbing species within a non-swelling porous material. Here, we used  
427 a linear isotherm to describe the solute adsorption onto the solid grains (see Section 2.2.1.2) and surface diffusion  
428 is neglected (no transport within the solid phase). The system is initially at thermodynamic equilibrium so that  
429 partitioning between gas and solid phases is respected. The adsorption and desorption kinetics coefficients  
430  $K_{att}$  and  $K_{det}$  are chosen high enough so that the equilibrium state is verified at each time step. Based on these  
431 assumptions, the 1D boundary value problem is defined as follows:

$$432 \quad \frac{\partial c}{\partial t} = D^K \frac{\delta^2 c}{\delta x^2}, \quad \forall x \in [0, L_0]$$

$$433 \quad s(x, t) = K_d c(x, t), \quad \forall x \in [0, L_0] \quad (45)$$

$$434 \quad c(x, 0) = c_0; s(x, 0) = K_d c_0, \quad \forall x \in [0, L_0]$$

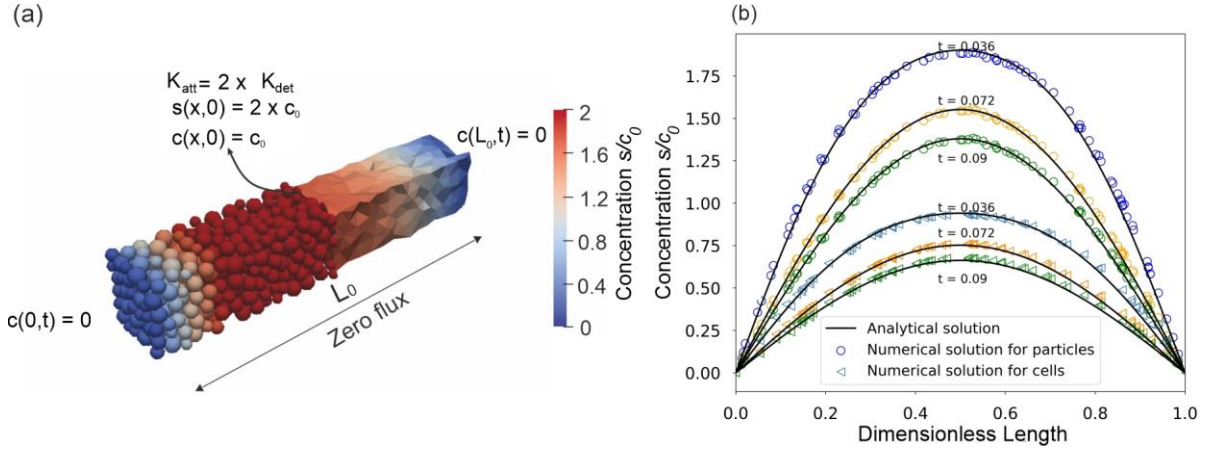
$$435 \quad c(0, t) = c(L_0, t) = 0$$

436 and the transient analytical solution is given by:

$$437 \quad c(x, t) = \sum_{m=1}^{\infty} \frac{2}{\pi} \left( \frac{1 - \cos(m\pi)}{m} \right) \sin \left( m\pi \frac{x}{L} \right) e^{-\left( \frac{D^K}{n_a(1+K_d)L_0^2} \right) (m\pi)^2 t_0} \quad (46)$$

438 The numerical parameters used for this test case are presented in Table 1. Figure 7a displays an example of the  
439 concentration fields in both pores and grains obtained at a given time while a comparison of the numerical  
440 solutions with a averaged concentration profiles at different times is provided in Figure 7b. Here a gain, a very good

441 agreement between the numerical and analytical solutions is obtained. We may also observe that our kinetics  
 442 formulation converges well to the equilibrium since the partitioning between gas and solid grains, driven by  $K_d =$   
 443 2, is always respected. This comparison validates the coupling method between diffusion and sorption processes.



444

445 Figure 7. a) Concentration distribution in particles and pores simulated numerically at  $t = 0.04$ . b) Comparison of numerical and analytical  
 446 concentration profiles in pores and particles at different times.

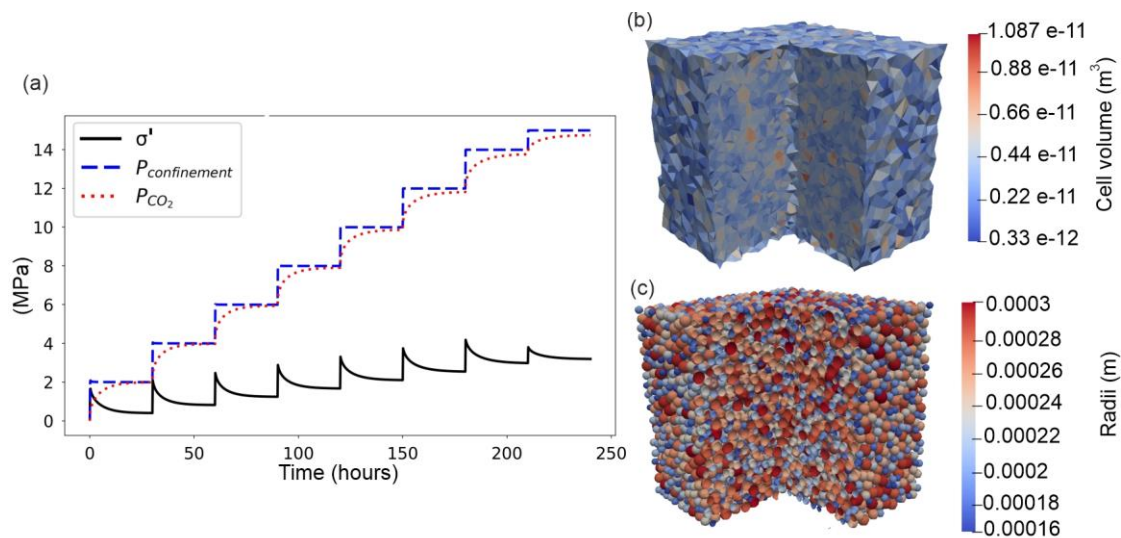
## 447 5 Hydro-mechanical behavior: comparison with a swelling experiment

448 To verify the implementation and validity of our HM scheme (Section 2.3), we compared the predictions of our  
 449 model to the experimental results of Day et al. (Day et al., 2008a) who performed a swelling experiment on a 30  
 450 x 10 x 10 mm block of coal under confined conditions. The CO<sub>2</sub>-induced coal swelling was measured for different  
 451 values of CO<sub>2</sub> pressure by optical method. The experiment performed at 55°C on the Australian bituminous coal  
 452 from the Bowen Basin (referred to as sample 3 in Day et al. (Day et al., 2008a) and as Qld8 in Day et al. (Day et  
 453 al., 2008b)) was used as reference. Note that the same data set (but at 40°C) was also used by (Sampath et al.,  
 454 2020) for model validation purpose but some discrepancies exist between our two investigations. Indeed, due to  
 455 the lack of experimental data available, a part of their numerical properties were obtained from another coal  
 456 experiment and they discarded the highest pressures of swelling experiment (higher than 12MPa) for comparison.  
 457 In the present analysis, we did our best to carry out a fair comparison by using the full range of experimental data  
 458 available and a complete set of consistent physical properties for this coal. All the parameter values are gathered  
 459 in Table 2. Because the elastic properties and Biot coefficient were not provided either in (Day et al., 2008b,  
 460 2008a), we set the value of  $b$  based on the value used by Sampath et al. (Sampath et al., 2020). The Young modulus  
 461  $E$  and the Poisson ratio  $\nu$  were chosen in order to reproduce the behavior observed by Day et al. (Day et al., 2008a)  
 462 with a non-sorbing gas (a volumetric contraction of 0.06% was reached at 15MPa of helium pressure). The  $s_{max}$

463 value was inferred from the maximum sorption capacity of the coal  $W_0$  in the isotherm model calculated by Day  
 464 et al. (Day et al., 2008b) (68.4 kg of CO<sub>2</sub> per ton of rock for the sample Qld 8). Finally, values of  $D^K$  and  $D^S$  were  
 465 taken from the literature (Dong et al., 2017) whereas  $K_{att}$ ,  $K_{det}$  were fixed arbitrarily.  $D^S$  is fixed constant but  $D^K$   
 466 varies as a function of the pore radius, as expressed in Equation (10), around an average value found in the  
 467 literature (see Table 2). Note that the values chosen for these transport and kinetic parameters do not affect the  
 468 steady-state behavior and hence, the comparison we made which is based on equilibrium states.

469 *5.1 Sample preparation*

470 A 10 x 10 x 10 mm particle assembly made up of 10,000 particles was generated and the interparticle properties  
 471 calibrated following the approach proposed by Scholtès and Donzé (Scholtès and Donzé, 2013). The coal sample  
 472 is considered isotropic although, even for the matrix, this assumption may be questioned (Day et al., 2008a). The  
 473 calibration was done by performing uniaxial compression tests on the numerical sample following a trial and  
 474 errors approach to determine the adequate interparticle properties to match both Young modulus and Poisson ratio  
 475 of the coal. In addition, both the porosity and Biot coefficient of the numerical sample were defined to match  
 476 those of the tested coal by following the procedures presented in Section 3.1.



477  
 478 Figure 8 Numerical set up for simulating the swelling experiment of Day et al. (2008): a) boundary pressures and resulting mean effective  
 479 stress, b) pore size distribution, c) particles size distribution.



480 Table 2

481 Numerical parameters used to simulate the coal matrix experiment by Day et al. [57]. The star symbol denotes  
 482 the calibration parameters.

Parameters	DEM-PFV model	Sources
Young modulus $E$ (GPa) *	4.550	<i>computed from Day et al., 2008 (Day et al., 2008a) (sample 3)</i>
Poisson ratio $\nu$ (-)*	0.225	<i>computed from Day et al., 2008 (Day et al., 2008a) (sample 3)</i>
Temperature $T$ (K)	328	<i>Day et al., 2008 (Day et al., 2008a) (sample 3)</i>
Gas constant $R$ (J.mol <sup>-1</sup> .K <sup>-1</sup> )	8.314	N/A
Molar mass $M_g$ (g.mol <sup>-1</sup> )	44.01	N/A
Bulk density (kg.m <sup>-3</sup> )	1220	<i>Day et al., 2008 (Day et al., 2008b) (sample Qld 8, Table 3)</i>
Skeletal density (kg.m <sup>-3</sup> )	1303	<i>Day et al., 2008 (Day et al., 2008b) (sample Qld 8, Table 3)</i>
$s_{max}$ (mol.m <sup>-3</sup> )	2025	<i>Day et al., 2008 (Day et al., 2008b) (sample Qld 8, Table 2)</i>
$K_d$ (mol.m <sup>-3</sup> ) *	0.0017	-
$K_{att}$ (s <sup>-1</sup> )	17e-11	-
$K_{det}$ (mol.m <sup>-3</sup> .s <sup>-1</sup> )	1e-7	-
$D^K$ (×10 <sup>-12</sup> m <sup>2</sup> .s <sup>-1</sup> )	3	<i>Dong et al., 2017 (Dong et al., 2017) (Table 4)</i>
$D^S$ (×10 <sup>-12</sup> m <sup>2</sup> .s <sup>-1</sup> )	30	<i>Dong et al., 2017 (Dong et al., 2017) (Table 4)</i>
Biot coefficient $b$ (-)	0.8	<i>Sampath et al., 2020 (Sampath et al., 2020) (Table 2)</i>
Coupling coefficient $\alpha$ (-) *	20.2	-
Porosity of assembly $n_a$ (%)	32	N/A
Porosity of coal sample $n_m$ (%)	7.1	<i>Day et al., 2008 (Day et al., 2008b) (sample Qld 8, Table 3)</i>

483 5.2 Experimental procedure

484 Day et al. (Day et al., 2008a) measured the dimensional changes of a sample contained within a pressure cell  
 485 where CO<sub>2</sub> pressure was increased up to 15 MPa. In our experiment, the numerical sample is confined in between  
 486 6 frictionless boundary walls to control the confining pressure  $p_{confinement}$ . To reproduce the swelling experiment  
 487 of Day et al. (Day et al., 2008a), we imposed CO<sub>2</sub> pressure both as boundary stress ( $p_{confinement}$ ) and as boundary  
 488 pressure ( $p_{CO_2}$ ) on all the sample boundaries.  $p_{confinement}$  is adjusted by displacing the boundary walls. During  
 489 the simulation,  $p_{CO_2}$  and  $p_{confinement}$  were increased stepwise from equilibrium states and the volumetric  
 490 deformation  $\epsilon_v$ , solvation pressure ( $p_s$ ), adsorbed amount of gas ( $s$ ) and fluid pressure ( $p_f$ ) were recorded at each  
 491 step (Figure 8a).

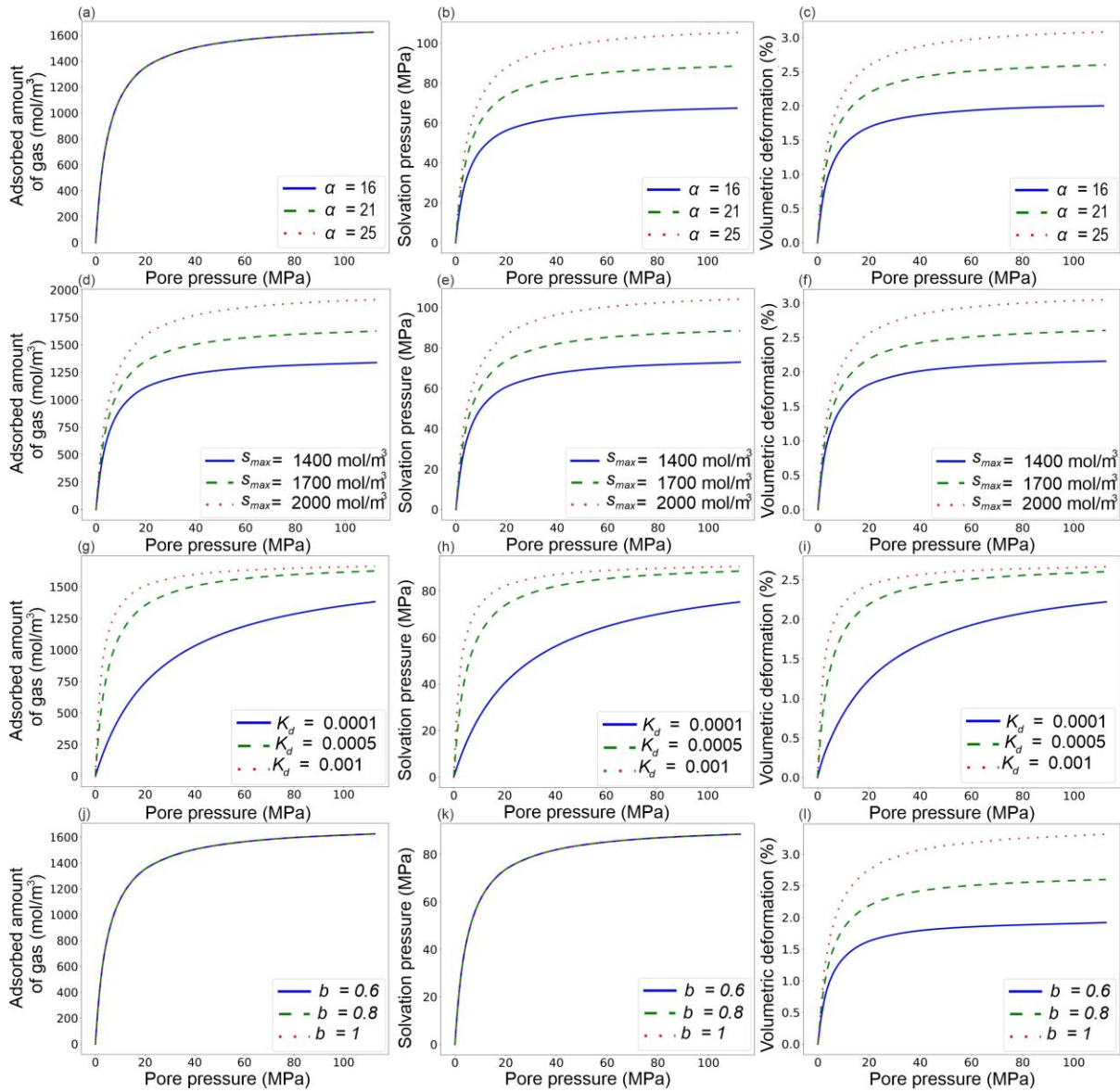
492 Since the Biot coefficient is lower than one, the effective stress varies at each CO<sub>2</sub> injection pressure step. Day et  
 493 al. (Day et al., 2008a) however suggest that the mechanical compression caused by the pore pressure increase can

494 be neglected (0.06% of contraction for non-sorbing gas against 2% of swelling deformation with CO<sub>2</sub> at 15Mpa).  
495 In other words, Day et al. investigated throughout this experiment the influence of sorption-induced swelling on  
496 the poromechanical behavior of the material without taking into consideration the effect of the fluid bulk pressure.

### 497 5.3 Parametric study

498 Before directly comparing the model results with the experimental observations, a parametric study is presented  
499 to highlight the influence of the model parameters on the emergent behavior. The results are summarized in Figure  
500 9 and the parameters roles assessed as follows:

- 501 • The coupling term  $\alpha$  controls the intensity of the solvation pressure  $p_s$  (Equation (30), Figure 9b), hence  
502 the amplitude of the associated deformation (Equation (35), Figure 9c). Thus,  $\alpha$  needs to be adjusted as  
503 a function of the swelling potential of the material with respect to the nature of the adsorbed fluid as, for  
504 example, CO<sub>2</sub> induces larger swelling than CH<sub>4</sub> in coal (Durucau et al., 2009).  $p_s$  is directly proportional  
505 to  $\alpha$  (Figure 9b), giving the opportunity to set its value so as to match experimental evidence of swelling  
506 for each combination of material and adsorbed fluid. One has to note that  $\alpha$  does not influence the amount  
507 of molecules that can be adsorbed on the solid phase (Figure 9a).
- 508 • According to Equations (15) and (16),  $s_{max}$  determines the maximum amount of gas molecules that can  
509 be adsorbed on the surfaces of the solid phase. Depending on the nature of the fluid-solid interaction at  
510 play,  $s_{max}$  must be adjusted because it also affects the solvation pressure and thus the volumetric  
511 deformation (Figure 9d-e-f). In contrast,  $K_d$  controls the adsorption/desorption kinetics (Figure 9g-h-i)  
512 without influencing the maximum amount of adsorbed gas molecules, hence leading to the same plateau  
513 value for the adsorbed amount of gas molecules, solvation pressure and volumetric deformation.
- 514 • Finally, the Biot coefficient  $b$  does not influence neither the amount of adsorbed gas molecules nor the  
515 solvation pressure (Figure 9j-k) while it directly influences the volumetric deformation (Figure 9l), as  
516 described by the poromechanical equation (Equation (35)).



517

518

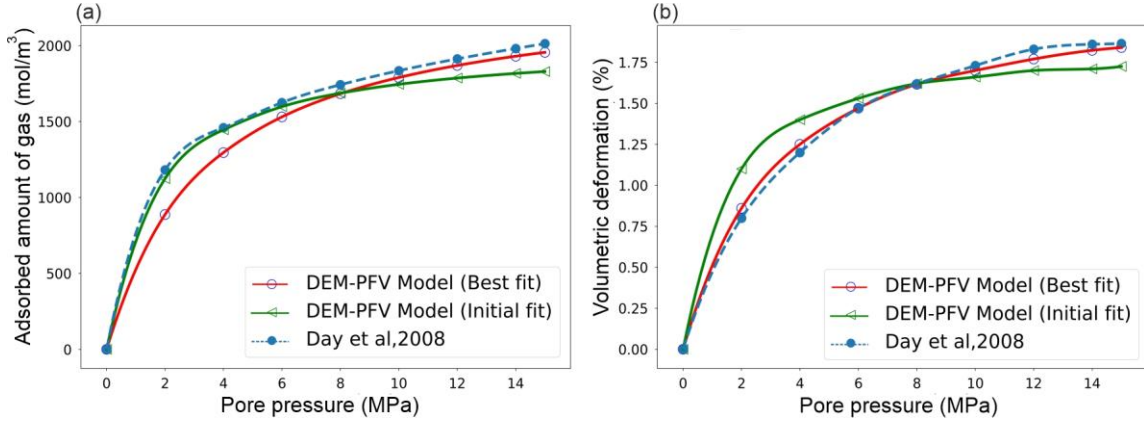
Figure 9 Evolution of adsorbed amount of gas  $s$  (left), solvation pressure  $p_s$  (middle) and volumetric deformation  $\varepsilon_v$  (right) versus pore pressure  $p_f$  for: (a,b,c) different  $\alpha$  values and fixed parameters ( $s_{max}=1700$ ,  $K_d=0.0005$ ,  $b=0.8$ ), (d,e,f) different  $s_{max}$  values and fixed parameters ( $\alpha=21$ ,  $K_d=0.0005$ ,  $b=0.8$ ), (g,h,i) different  $K_d$  values and fixed parameters ( $\alpha=21$ ,  $s_{max}=1700$ ,  $b=0.8$ ), (j,k,l) different  $b$  values

520

and fixed parameters ( $\alpha=21$ ,  $K_d=0.0005$ ,  $s_{max}=1700$ ).

521

and fixed parameters ( $\alpha=21$ ,  $K_d=0.0005$ ,  $s_{max}=1700$ ).



523

524 Figure 10 Swelling experiment: comparison of the DEM-PFV model predictions to the experiment of Day et al. (Day et al., 2008a):

525 evolutions of a) adsorbed amount of gas and, b) volumetric deformation as functions of the pore pressure.

526 The calibration of the model was done through the following procedure:

- 527 1. Determine the interparticle elastic properties ( $E_{eq}$  and  $P$ ) through uniaxial or triaxial compression testing
- 528 (trial and error adjustments) to match both Young modulus  $E$  and Poisson ratio  $\nu$  of the material.
- 529 2. Set  $b$  equal to the measured value and scale the numerical sample connected porosity  $n_{a,c}$ .
- 530 3. Determine the experimental solvation pressure  $p_s$  by using the extended poromechanical equations,
- 531 (Equations (35) and (36)) such that

$$532 \quad p_s = \frac{K \varepsilon_v + (\sigma - b p_f)}{b} \quad (47)$$

533 where  $K = \frac{E}{3(1-2\nu)}$  is the bulk modulus and  $\sigma = \frac{\sigma_{kk}}{3}$  is the mean stress and, from the value of  $s_{max}$ ,

534 estimate  $\alpha$  using the plateau value of  $p_s$ .

- 535 4. Finally, calibrate  $K_d$  (trial and error adjustments) so that the numerical results fit with the experiments in
- 536 terms of solvation pressure or swelling deformation.

537 The numerical results presented in Figure 10 (referred to as the initial fit) match the experimental observations

538 for the following set of parameters:  $\alpha = 20.02$ ,  $K_d = 0.0017 \text{ mol.m}^{-3}$  with the  $s_{max}$  value inferred from the

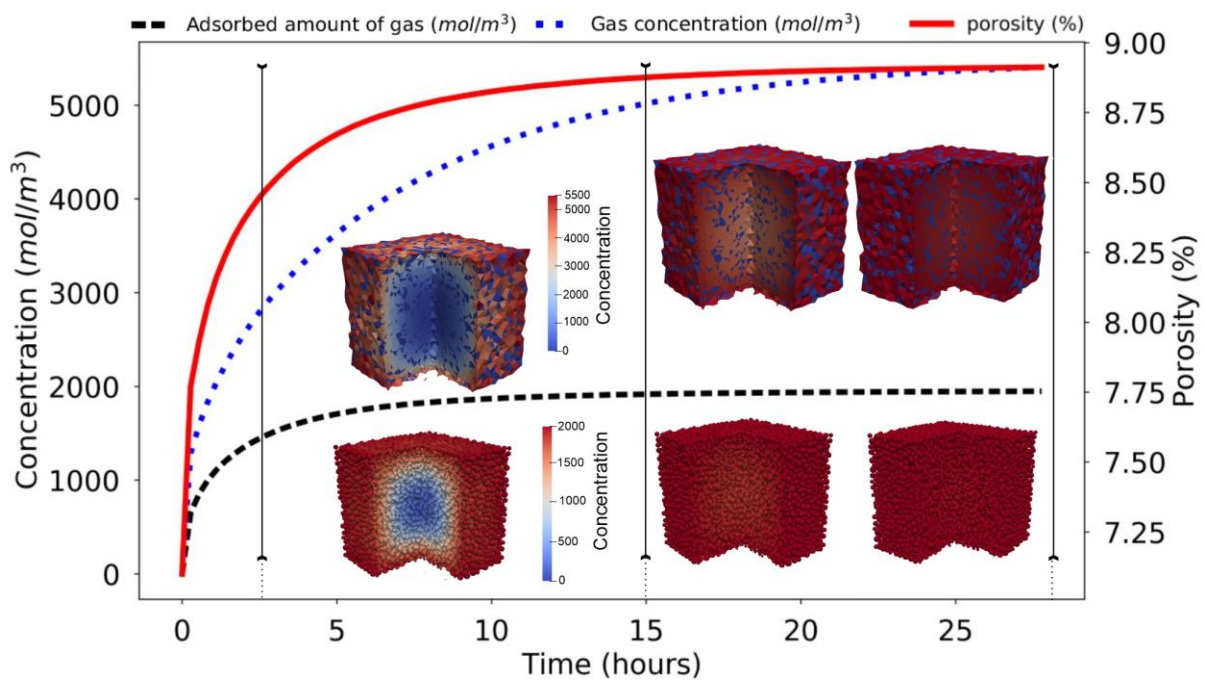
539 experiment ( $s_{max} = 2025 \text{ mol.m}^{-3}$ ). The fit to experimental data point is not ideal yet. In their study, Day et al.

540 (Day et al., 2008b) have explored a pore filling isotherm model (Dubinin–Radushkevich model) which has been

541 found to provide a better fit to experimental adsorption data than the classical Langmuir model, especially at high

542 pressures, above 6 MPa. A comparison between this isotherm model and ours is shown in Figure 10a and confirms  
 543 this observation. This discrepancy, inherent to the use of Langmuir isotherm model, is also observed when  
 544 comparing volumetric deformations in Figure 10b (an average error of 19% is found). Note that a better fit can be  
 545 achieved when fitting also the  $s_{max}$  value. A second simulation, referred to as the best fit, where  $s_{max} = 2400$   
 546  $\text{mol}\cdot\text{m}^{-3}$ ,  $K_d = 0.0008 \text{ mol}\cdot\text{m}^{-3}$  and  $\alpha = 20.02$  are shown in Figure 10a and Figure 10b. The error is thus reduced  
 547 to 2%.

548 Additional insights can be gained from numerical simulations into the dynamics of mass transfer processes within  
 549 the coal material. Figure 11 shows the changes in averaged gas and sorbed concentrations with time in the porous  
 550 sample between two successive constant pressure steps. The corresponding porosity variation is also exhibited.  
 551 As an illustrative example, we focused on the transient behavior corresponding to an increase from 0 to 15 MPa  
 552 of  $\text{CO}_2$  pressure. Results indicate that the gas diffuses first through the solid phase. As expected from diffusion  
 553 values of Table 2 and accordingly to the literature (Dong et al., 2017; Mathias et al., 2020), surface diffusion is  
 554 the predominant transport mechanism within coal matrix. This increase in sorbed concentration within the coal  
 555 sample results in swelling and hence, volumetric strain and porosity increase. Owing to the values used for  $K_{att}$   
 556 and  $K_{det}$ , the desorption rate is not large enough and equilibrium is reached faster in the solid phase than in the gas  
 557 phase (Figure 11). As a consequence, swelling occurs before the pore pressure reaches its equilibrium state in  
 558 agreement with Sampath et al. results (Sampath et al., 2020).



559

560

Figure 11. Evolution of porosity, fluid concentration and adsorbed amount of gas with time.

## 561 **6 Conclusion**

562 A new 3D pore-scale model for porous swelling materials is proposed to investigate coal bed methane production.

563 In our model, a DEM model where the material is represented as an assembly of particles interacting one with

564 another according to predefined contact laws is coupled to a PNM approach for describing transport mechanisms

565 between and within pores and solid grains. The material is assumed to be saturated with gas and various

566 mechanisms for gas transport across the coal matrix have been considered including Knudsen diffusion, surface

567 diffusion and sorption. Mechanical couplings inherent to such swelling materials are also taken into account. The

568 model simulates both (i) the interplay between pore pressure and external stress with variations in the effective

569 stress which may impact the mechanical behavior of the medium and (ii) the sorption processes which contribute

570 to swell or shrink the material. This latter mechanism is considered through the addition of an additional pressure

571 term, classically called the solvation pressure, related to the sorbed concentration.

572 The implementation of the model was tested against analytical solutions and compared to a swelling experiment.

573 The model was found to be robust and a suitable tool for describing adsorption induced deformation. This

574 comprehensive investigation reveals the complex physics at stake during methane adsorption and the numerical

575 results give precious insights onto the internal dynamics of gas within the coal matrix. In particular, simulations

576 reveal that coal matrix swelling occurs before the pore pressure reaches its equilibrium state since surface diffusion

577 prevails. The present model is thus capable to describe the strong coupling between transport, chemical (sorption)

578 and mechanical processes and can be used to predict methane recovery. Future work will focus on introducing

579 cleat network to assess the effect of cleat intensity and facilitate more comprehensive analysis on the permeability

580 changes at the coal rock mass scale.

581

582 **Acknowledgments:** This study was conducted in the framework of a research and development project, Regalor

583 (Ressources Gazières de Lorraine), carried by GeoRessources laboratory (Université de Lorraine— CNRS) on

584 Grand-Est region's initiative and supported by the European Regional Development Fund.

585

- 587 Bertrand, F., Cerfontaine, B., Collin, F., 2017. A fully coupled hydro-mechanical model for the modeling of  
588 coalbed methane recovery. *J. Nat. Gas Sci. Eng.* 46, 307–325.  
589 <https://doi.org/10.1016/j.jngse.2017.07.029>
- 590 Biot, M.A., 1941. General Theory of Three-Dimensional Consolidation. *J. Appl. Phys.* 12, 155–164.  
591 <https://doi.org/10.1063/1.1712886>
- 592 Brochard, L., Vandamme, M., Pellenq, R.J.-M., 2012. Poromechanics of microporous media. *J. Mech. Phys.*  
593 *Solids* 60, 606–622. <https://doi.org/10.1016/j.jmps.2012.01.001>
- 594 Catalano, E., Chareyre, B., Barthélémy, E., 2014. Pore-scale modeling of fluid-particles interaction and  
595 emerging poromechanical effects. *Int. J. Numer. Anal. Methods Geomech.* 38, 51–71.  
596 <https://doi.org/10.1002/nag.2198>
- 597 Caulk, R., Scholtès, L., Krzaczek, M., Chareyre, B., 2020. A pore-scale thermo–hydro-mechanical model for  
598 particulate systems. *Comput. Methods Appl. Mech. Eng.* 372, 113292.  
599 <https://doi.org/10.1016/j.cma.2020.113292>
- 600 Ceglarska-Stefańska, G., Czapliński, A., 1993. Correlation between sorption and dilatometric processes in hard  
601 coals. *Fuel* 72, 413–417. [https://doi.org/10.1016/0016-2361\(93\)90064-9](https://doi.org/10.1016/0016-2361(93)90064-9)
- 602 Ceglarska-Stefańska, G., Zarębska, K., 2002. The competitive sorption of CO<sub>2</sub> and CH<sub>4</sub> with regard to the  
603 release of methane from coal. *Fuel Process. Technol.* 77–78, 423–429. [https://doi.org/10.1016/S0378-3820\(02\)00093-0](https://doi.org/10.1016/S0378-3820(02)00093-0)
- 604
- 605 Chareyre, B., Cortis, A., Catalano, E., Barthélémy, E., 2012. Pore-Scale Modeling of Viscous Flow and Induced  
606 Forces in Dense Sphere Packings. *Transp. Porous Media* 94, 595–615. <https://doi.org/10.1007/s11242-012-0057-2>
- 607
- 608 Choi, J.-G., Do, D.D., Do, H.D., 2001. Surface Diffusion of Adsorbed Molecules in Porous Media: Monolayer,  
609 Multilayer, and Capillary Condensation Regimes. *Ind. Eng. Chem. Res.* 40, 4005–4031.  
610 <https://doi.org/10.1021/ie010195z>
- 611 Connell, L.D., 2016. A new interpretation of the response of coal permeability to changes in pore pressure,  
612 stress and matrix shrinkage. *Int. J. Coal Geol.* 162, 169–182. <https://doi.org/10.1016/j.coal.2016.06.012>
- 613 Cundall, P.A., Strack, O.D.L., 1979. A discrete numerical model for granular assemblies. *Géotechnique* 29, 47–  
614 65. <https://doi.org/10.1680/geot.1979.29.1.47>
- 615 Day, S., Duffy, G., Sakurovs, R., Weir, S., 2008b. Effect of coal properties on CO<sub>2</sub> sorption capacity under  
616 supercritical conditions. *Int. J. Greenh. Gas Control*, EGU General Assembly 2007: Advances in CO<sub>2</sub>  
617 Storage in Geological Systems 2, 342–352. [https://doi.org/10.1016/S1750-5836\(07\)00120-X](https://doi.org/10.1016/S1750-5836(07)00120-X)
- 618 Day, S., Fry, R., Sakurovs, R., 2008a. Swelling of Australian coals in supercritical CO<sub>2</sub>. *Int. J. Coal Geol.* 74,  
619 41–52. <https://doi.org/10.1016/j.coal.2007.09.006>
- 620 Detournay, E., Cheng, A.H.-D., 1993. 5 - Fundamentals of Poroelasticity, in: Fairhurst, C. (Ed.), *Analysis and*  
621 *Design Methods*. Pergamon, Oxford, pp. 113–171. <https://doi.org/10.1016/B978-0-08-040615-2.50011-3>
- 622
- 623 Dilatation of Porous Glass - SCHERER - 1986 - Journal of the American Ceramic Society - Wiley Online  
624 Library [WWW Document], n.d. URL  
625 <https://ceramics.onlinelibrary.wiley.com/doi/abs/10.1111/j.1151-2916.1986.tb07448.x> (accessed  
626 11.14.22).
- 627 Do, D.D., 1998. Adsorption Analysis: Equilibria And Kinetics (With Cd Containing Computer Matlab  
628 Programs). World Scientific.
- 629 Dolino, G., Bellet, D., Faivre, C., 1996. Adsorption strains in porous silicon. *Phys. Rev. B* 54, 17919–17929.  
630 <https://doi.org/10.1103/PhysRevB.54.17919>
- 631 Dong, J., Cheng, Y., Liu, Q., Zhang, H., Zhang, K., Hu, B., 2017. Apparent and True Diffusion Coefficients of  
632 Methane in Coal and Their Relationships with Methane Desorption Capacity. *Energy Fuels* 31, 2643–  
633 2651. <https://doi.org/10.1021/acs.energyfuels.6b03214>
- 634 Duriez, J., Scholtès, L., Donzé, F.-V., 2016. Micromechanics of wing crack propagation for different flaw  
635 properties. *Eng. Fract. Mech.* 153, 378–398. <https://doi.org/10.1016/j.engfracmech.2015.12.034>
- 636 Durucan, S., Ahsanb, M., Shia, J.-Q., 2009. Matrix shrinkage and swelling characteristics of European coals.  
637 *Energy Procedia, Greenhouse Gas Control Technologies* 9 1, 3055–3062.  
638 <https://doi.org/10.1016/j.egypro.2009.02.084>
- 639 Espinoza, D.N., Vandamme, M., Dangla, P., Pereira, J.-M., Vidal-Gilbert, S., 2013. A transverse isotropic  
640 model for microporous solids: Application to coal matrix adsorption and swelling. *J. Geophys. Res.*  
641 *Solid Earth* 118, 6113–6123. <https://doi.org/10.1002/2013JB010337>

642 Espinoza, D.N., Vandamme, M., Pereira, J.-M., Dangla, P., Vidal-Gilbert, S., 2014. Measurement and modeling  
643 of adsorptive–poromechanical properties of bituminous coal cores exposed to CO<sub>2</sub>: Adsorption,  
644 swelling strains, swelling stresses and impact on fracture permeability. *Int. J. Coal Geol.* 134–135, 80–  
645 95. <https://doi.org/10.1016/j.coal.2014.09.010>

646 Gor, G.Yu., Neimark, A.V., 2010. Adsorption-Induced Deformation of Mesoporous Solids. *Langmuir* 26,  
647 13021–13027. <https://doi.org/10.1021/la1019247>

648 Grosman, A., Ortega, C., 2008. Influence of elastic deformation of porous materials in adsorption-desorption  
649 process: A thermodynamic approach. *Phys. Rev. B* 78, 085433.  
650 <https://doi.org/10.1103/PhysRevB.78.085433>

651 Guo, X., Wang, Z., Zhao, Y., 2016. A comprehensive model for the prediction of coal swelling induced by  
652 methane and carbon dioxide adsorption. *J. Nat. Gas Sci. Eng.* 36, 563–572.  
653 <https://doi.org/10.1016/j.jngse.2016.10.052>

654 Jing, Y., Armstrong, R.T., Ramandi, H.L., Mostaghimi, P., 2017. Topological Characterization of Fractured  
655 Coal. *J. Geophys. Res. Solid Earth* 122, 9849–9861. <https://doi.org/10.1002/2017JB014667>

656 Kowalczyk, P., Ciach, A., Neimark, A.V., 2008. Adsorption-Induced Deformation of Microporous Carbons:  
657 Pore Size Distribution Effect. *Langmuir* 24, 6603–6608. <https://doi.org/10.1021/la800406c>

658 Laubach, S.E., Marrett, R.A., Olson, J.E., Scott, A.R., 1998. Characteristics and origins of coal cleat: A review.  
659 *Int. J. Coal Geol.* 35, 175–207. [https://doi.org/10.1016/S0166-5162\(97\)00012-8](https://doi.org/10.1016/S0166-5162(97)00012-8)

660 Li, Z., Liu, D., Cai, Y., Ranjith, P.G., Yao, Y., 2017. Multi-scale quantitative characterization of 3-D pore-  
661 fracture networks in bituminous and anthracite coals using FIB-SEM tomography and X-ray  $\mu$ -CT.  
662 *Fuel* 209, 43–53. <https://doi.org/10.1016/j.fuel.2017.07.088>

663 Liu, J., Chen, Z., Elsworth, D., Qu, H., Chen, D., 2011. Interactions of multiple processes during CBM  
664 extraction: A critical review. *Int. J. Coal Geol.* 87, 175–189. <https://doi.org/10.1016/j.coal.2011.06.004>

665 Liu, L., Luo, X.-B., Ding, L., Luo, S.-L., 2019. 4 - Application of Nanotechnology in the Removal of Heavy  
666 Metal From Water, in: Luo, X., Deng, F. (Eds.), *Nanomaterials for the Removal of Pollutants and*  
667 *Resource Reutilization, Micro and Nano Technologies.* Elsevier, pp. 83–147.  
668 <https://doi.org/10.1016/B978-0-12-814837-2.00004-4>

669 Liu, M., Mostaghimi, P., 2017. Pore-scale modelling of CO<sub>2</sub> storage in fractured coal. *Int. J. Greenh. Gas*  
670 *Control* 66, 246–253. <https://doi.org/10.1016/j.ijggc.2017.09.007>

671 Ma, T., Rutqvist, J., Oldenburg, C.M., Liu, W., 2017. Coupled thermal–hydrological–mechanical modeling of  
672 CO<sub>2</sub>-enhanced coalbed methane recovery. *Int. J. Coal Geol.* 179, 81–91.  
673 <https://doi.org/10.1016/j.coal.2017.05.013>

674 Majewska, Z., Majewski, S., Ziętek, J., 2010. Swelling of coal induced by cyclic sorption/desorption of gas:  
675 Experimental observations indicating changes in coal structure due to sorption of CO<sub>2</sub> and CH<sub>4</sub>. *Int. J.*  
676 *Coal Geol.* 83, 475–483. <https://doi.org/10.1016/j.coal.2010.07.001>

677 Mathias, S.A., Dentz, M., Liu, Q., 2020. Gas Diffusion in Coal Powders is a Multi-rate Process. *Transp. Porous*  
678 *Media* 131, 1037–1051. <https://doi.org/10.1007/s11242-019-01376-x>

679 Mostaghimi, P., Armstrong, R.T., Gerami, A., Hu, Y., Jing, Y., Kamali, F., Liu, M., Liu, Z., Lu, X., Ramandi,  
680 H.L., Zamani, A., Zhang, Y., 2017. Cleat-scale characterisation of coal: An overview. *J. Nat. Gas Sci.*  
681 *Eng.* 39, 143–160. <https://doi.org/10.1016/j.jngse.2017.01.025>

682 Mostaghimi, P., Armstrong, R.T., Gerami, A., Hu, Y., Jing, Y., Kamali, F., Liu, M., Liu, Z., Lu, X., Ramandi,  
683 H.L., Zamani, A., Zhang, Y., 2016. Pore Scale Characterisation of Coal: An Unconventional  
684 Challenge. Presented at the Abu Dhabi International Petroleum Exhibition & Conference, OnePetro.  
685 <https://doi.org/10.2118/183411-MS>

686 Mushrif, S.H., Rey, A.D., 2009. An integrated model for adsorption-induced strain in microporous solids.  
687 *Chem. Eng. Sci.*, *Morton Denn Festschrift* 64, 4744–4753. <https://doi.org/10.1016/j.ces.2009.04.014>

688 Nikoosokhan, S., Vandamme, M., Dangla, P., 2014. A poromechanical model for coal seams saturated with  
689 binary mixtures of CH<sub>4</sub> and CO<sub>2</sub>. *J. Mech. Phys. Solids* 71, 97–111.  
690 <https://doi.org/10.1016/j.jmps.2014.07.002>

691 Ottiger, S., Pini, R., Storti, G., Mazzotti, M., 2008. Competitive adsorption equilibria of CO<sub>2</sub> and CH<sub>4</sub> on a dry  
692 coal. *Adsorption* 14, 539–556. <https://doi.org/10.1007/s10450-008-9114-0>

693 Pan, Z., Connell, L.D., 2007. A theoretical model for gas adsorption-induced coal swelling. *Int. J. Coal Geol.*  
694 69, 243–252. <https://doi.org/10.1016/j.coal.2006.04.006>

695 Papachristos, E., Scholtès, L., Donzé, F.V., Chareyre, B., 2017. Intensity and volumetric characterizations of  
696 hydraulically driven fractures by hydro-mechanical simulations. *Int. J. Rock Mech. Min. Sci.* 93, 163–  
697 178. <https://doi.org/10.1016/j.ijrmms.2017.01.011>



698 Perrier, L., Pijaudier-Cabot, G., Grégoire, D., 2018. Extended poromechanics for adsorption-induced swelling  
699 prediction in double porosity media: Modeling and experimental validation on activated carbon. *Int. J.*  
700 *Solids Struct.* 146, 192–202. <https://doi.org/10.1016/j.ijsolstr.2018.03.029>

701 Pijaudier-Cabot, G., Vermorel, R., Miqueu, C., Mendiboure, B., 2011. Revisiting poromechanics in the context  
702 of microporous materials. *Comptes Rendus Mécanique* 339, 770–778.  
703 <https://doi.org/10.1016/j.crme.2011.09.003>

704 Pini, R., Ottiger, S., Burlini, L., Storti, G., Mazzotti, M., 2009. Role of adsorption and swelling on the dynamics  
705 of gas injection in coal. *J. Geophys. Res. Solid Earth* 114. <https://doi.org/10.1029/2008JB005961>

706 Privalov, V., Pironon, J., de Donato, P., Michels, R., Morlot, C., Izart, A., 2020. Natural Fracture Systems in  
707 CBM Reservoirs of the Lorraine–Saar Coal Basin from the Standpoint of X-ray Computer  
708 Tomography. *Environ. Sci. Proc.* 5, 12. <https://doi.org/10.3390/IECG2020-08772>

709 Raoof, A., Nick, H.M., Wolterbeek, T.K.T., Spiers, C.J., 2012. Pore-scale modeling of reactive transport in  
710 wellbore cement under CO<sub>2</sub> storage conditions. *Int. J. Greenh. Gas Control, CATO: CCS Research in*  
711 *the Netherlands* 11, S67–S77. <https://doi.org/10.1016/j.ijggc.2012.09.012>

712 Reinecke, S.A., Sleep, B.E., 2002. Knudsen diffusion, gas permeability, and water content in an unconsolidated  
713 porous medium. *Water Resour. Res.* 38, 16-1-16–15. <https://doi.org/10.1029/2002WR001278>

714 Sampath, K.H.S.M., Perera, M.S.A., Matthai, S.K., Ranjith, P.G., Dong-yin, L., 2020. Modelling of fully-  
715 coupled CO<sub>2</sub> diffusion and adsorption-induced coal matrix swelling. *Fuel* 262, 116486.  
716 <https://doi.org/10.1016/j.fuel.2019.116486>

717 Scholtès, L., Chareyre, B., Michallet, H., Catalano, E., Marzougui, D., 2015. Modeling wave-induced pore  
718 pressure and effective stress in a granular seabed. *Contin. Mech. Thermodyn.* 27, 305–323.  
719 <https://doi.org/10.1007/s00161-014-0377-2>

720 Scholtès, L., Donzé, F.-V., 2013. A DEM model for soft and hard rocks: Role of grain interlocking on strength.  
721 *J. Mech. Phys. Solids* 61, 352–369. <https://doi.org/10.1016/j.jmps.2012.10.005>

722 Šmilauer, V., Chareyre, B., Duriez, J., Eulitz, A., Gladky, A., Guo, N., Jakob, C., Kozicki, J., Kneib, F.,  
723 Modenese, C., Stransky, J., Thoeni, K., 2015. *Using and Programming*.  
724 <https://doi.org/10.5281/zenodo.34043>

725 Thorstenson, D.C., Pollock, D.W., 1989. Gas transport in unsaturated zones: Multicomponent systems and the  
726 adequacy of Fick's laws. *Water Resour. Res.* 25, 477–507. <https://doi.org/10.1029/WR025i003p00477>

727 Ustinov, E.A., Do, D.D., 2006. Effect of adsorption deformation on thermodynamic characteristics of a fluid in  
728 slit pores at sub-critical conditions. *Carbon* 44, 2652–2663.  
729 <https://doi.org/10.1016/j.carbon.2006.04.015>

730 Vermorel, R., Pijaudier-Cabot, G., 2014. Enhanced continuum poromechanics to account for adsorption induced  
731 swelling of saturated isotropic microporous materials. *Eur. J. Mech. - ASolids* 44, 148–156.  
732 <https://doi.org/10.1016/j.euromechsol.2013.10.010>

733 Wang, S., Elsworth, D., Liu, J., 2011. Permeability evolution in fractured coal: The roles of fracture geometry  
734 and water-content. *Int. J. Coal Geol.* 87, 13–25. <https://doi.org/10.1016/j.coal.2011.04.009>

735 Wang, Z., Cheng, Y., Zhang, K., Hao, C., Wang, L., Li, W., Hu, B., 2018. Characteristics of microscopic pore  
736 structure and fractal dimension of bituminous coal by cyclic gas adsorption/desorption: An  
737 experimental study. *Fuel* 232, 495–505. <https://doi.org/10.1016/j.fuel.2018.06.004>

738 Wu, Y., Liu, J., Elsworth, D., Chen, Z., Connell, L., Pan, Z., 2010. Dual poroelastic response of a coal seam to  
739 CO<sub>2</sub> injection. *Int. J. Greenh. Gas Control* 4, 668–678. <https://doi.org/10.1016/j.ijggc.2010.02.004>

740 Yang, K., Lu, X., Lin, Y., Neimark, A.V., 2010. Deformation of Coal Induced by Methane Adsorption at  
741 Geological Conditions. *Energy Fuels* 24, 5955–5964. <https://doi.org/10.1021/ef100769x>

742 Youjun, J., Vafai, K., 2017. Analysis of pore scale fluid migration in a porous medium - application to coal rock  
743 seam. *Int. J. Numer. Methods Heat Fluid Flow* 27, 1706–1719. <https://doi.org/10.1108/HFF-05-2016-0198>

744  
745